Beyond Point Masses. V. Weywot's Non-Keplerian Orbit

Benjamin Proudfoot[1] , Will Grundy[2,3] , Darin Ragozzine[4] , and Estela Fernández-Valenzuela[1]

[1] Florida Space Institute, University of Central Florida, 12354 Research Parkway, Orlando, FL 32826, USA; benp175@gmail.com
[2] Lowell Observatory, 1400 West Mars Hill Road, Flagstaff, AZ 86001, USA
[3] Northern Arizona University, Department of Astronomy & Planetary Science, PO Box 6010, Flagstaff, AZ 86011, USA
[4] Brigham Young University Department of Physics & Astronomy, N283 ESC, Brigham Young University, Provo, UT 84602, USA

Abstract

We present a detailed dynamical analysis of the Quaoar–Weywot system based on nearly 20 yr of high-precision astrometric data, including new Hubble Space Telescope observations and stellar occultations. Our study reveals that Weywot's orbit deviates significantly from a purely Keplerian model, requiring the inclusion of Quaoar's nonspherical gravitational field and center-of-body–center-of-light (COB-COL) offsets in our orbit models. We place a robust upper limit on Weywot's orbital eccentricity ($e < 0.02$), substantially lower than previous estimates, which has important implications for the strength of mean-motion resonances acting on Quaoar's ring system. Under the assumption that Quaoar's rings lie in its equatorial plane, we detect Quaoar's dynamical oblateness, J_2, at $\sim 2\sigma$ confidence. The low J_2 value found under that assumption implies that Quaoar is differentiated, with a total bulk density of 1751 ± 13 (stat.) $\mathrm{kg\,m^{-3}}$. Additionally, we detect significant COB-COL offsets likely arising from latitudinal albedo variations across Quaoar's surface. These offsets are necessary to achieve a statistically robust orbit fit and highlight the importance of accounting for surface heterogeneity when modeling the orbits of dwarf planet moons. These findings improve our understanding of Quaoar's interior and surface while providing key insights into the stability and confinement mechanisms of its rings.

Materials only available in the online version of record: *machine-readable table*

1. Introduction

The dwarf planet Quaoar is one of the most intriguing bodies yet discovered in the trans-Neptunian region. Like other large trans-Neptunian objects (TNOs), Quaoar hosts a relatively small moon—Weywot—discovered almost two decades ago in data from the Hubble Space Telescope (HST; M. E. Brown & T. A. Suer 2007). In addition, recent observations of stellar occultations by Quaoar show the existence of two rings orbiting outside of Quaoar's Roche limit (B. Morgado et al. 2023; C. Pereira et al. 2023). Repeated observations of these enigmatic rings have revealed that both appear to have substantial azimuthal structure, which has been interpreted as arc-like structures embedded within the rings. This is similar to the ring arcs seen in Neptune's Adams ring. These arcs are possibly caused by resonances with either Quaoar's spin–orbit resonances (SORs) or Weywot's mean-motion resonances (MMRs). Understanding how these rings formed, are confined, and have not accreted/dissipated is the subject of intense interest (e.g., A. Rodríguez et al. 2023; R. Ikeya & N. Hirata 2024). Given this interest, characterization of Quaoar's dynamical environment is crucial.

Quaoar's dynamical environment is dominated by both Weywot's orbital influence (especially near MMRs) and Quaoar's nonspherical gravitational field (especially near SORs). The ring system appears to be embedded within/near several of these resonances, with the outer ring—referred to as Q1R—located near Weywot's 6:1 MMR and Quaoar's 3:1

SOR (B. Morgado et al. 2023). Likewise, the inner ring—Q2R—is located near Weywot's 12:1 MMR and Quaoar's 7:5 SOR (C. Pereira et al. 2023; B. Proudfoot et al. 2025). We show a to-scale schematic of the Quaoar system, along with its SORs and MMRs, in Figure 1. For a more detailed descriptions of the resonances near Q1R, we refer the reader to Section 7. Understanding the relative strength and location of these resonances is central to understanding the ring system.

Weywot's MMRs are dependent on its mass and orbital parameters, while Quaoar's SORs are dependent on the shape of Quaoar's presumably triaxial gravitational field. Unfortunately, to date, strong constraints have not been able to be placed on almost all relevant parameters. Importantly, Weywot's orbit has yet to be fully constrained. Since the first publications on Weywot's orbit, almost every subsequent study has yielded notably different system mass, orbital period, and/or eccentricity estimates (e.g., W. C. Fraser & M. E. Brown 2010; F. Vachier et al. 2012; B. Morgado et al. 2023), underscoring the difficulty of achieving a consistent solution. These values are strongly related to the locations and strengths of the MMRs. Likewise, the shape of Quaoar's gravitational field remains unconstrained. Some 3D shape models of Quaoar have been published (C. Kiss et al. 2024; G. Margoti 2024), but these only place bounds on the shape of Quaoar's gravitational field.

Characterizing the dynamical environment of Quaoar is best achieved by precise astrometric tracking of Weywot's position. This allows Weywot to act as a probe of Quaoar's gravitational field while precisely characterizing the dynamical contributions from Weywot. This allows us to simultaneously constrain the properties of both Quaoar's SORs and Weywot's MMRs.
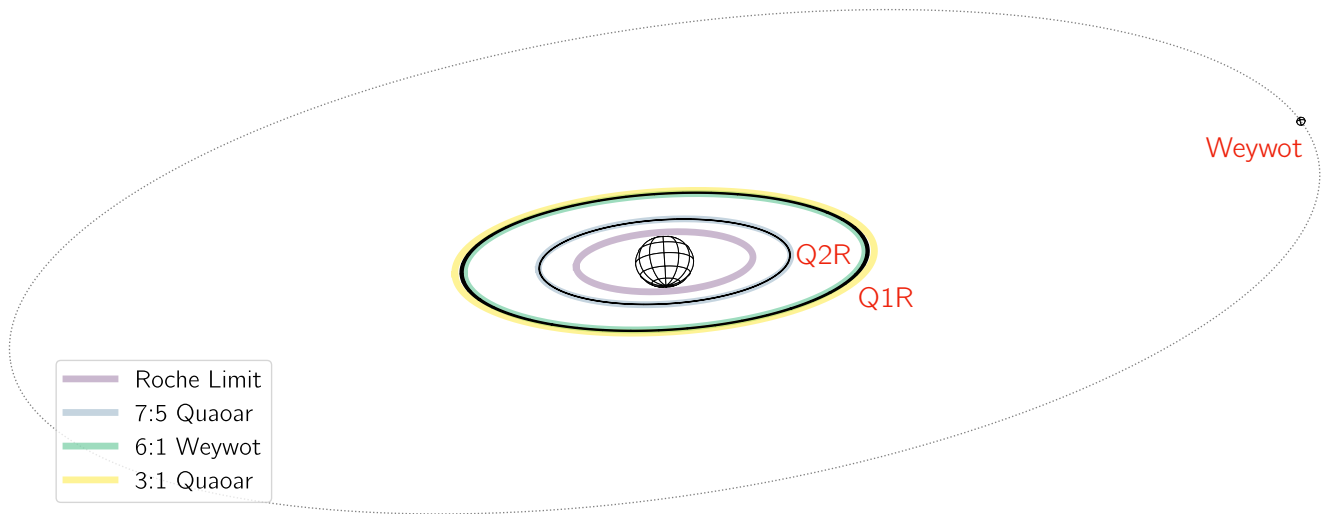
Figure 1. The architecture of the Quaoar system, as seen from Earth, shown to scale on 2006 September 21 12:00 UT. Locations of various SORs and MMRs are shown as colored ellipses. Quaoar's pole orientation, ring width, and ring orientation are based on B. Proudfoot et al. (2025). Quaoar's shape is based on G. Margoti (2024), although the rotational phase is unknown, but selected to be at light-curve maximum. Weywot's diameter is from E. Fernandez-Valenzuela et al. (2025, in preparation). Weywot's orbit is from this work.

In this work, we parameterize Quaoar's nonspherical gravitational field using a spherical harmonic expansion. The nonspherical potential (U) of Quaoar (with mass M) at a distance (r) can be written to quadrupole order as

$$U(r, \theta, \phi) = -\frac{GM}{r}\left[1 - J_2\left(\frac{R}{r}\right)^2\left(\frac{3}{2}\sin^2\theta - \frac{1}{2}\right) \right.$$
$$\left. + C_{22}\left(\frac{R}{r}\right)^2\cos^2\theta \sin 2\phi + \mathcal{O}(r^{-3}) \right], \quad (1)$$

where J_2 and C_{22} are the quadrupole-order gravitational harmonic coefficients, θ is the body-fixed latitude, ϕ is the body-fixed longitude, and R is the "reference" radius (C. F. Yoder 1995; D. Scheeres et al. 2000).[5] The term J_2 corresponds to the oblate potential of Quaoar, which causes "splitting" of Weywot's MMRs into distinct subresonances. Measuring Quaoar's J_2 is therefore important for understanding the dynamical state of Quaoar's rings. In contrast with J_2, C_{22} corresponds to a rotating prolate potential aligned with Quaoar's long axis. The value of C_{22} is directly related to the strength of Quaoar's SORs. Both J_2 and C_{22} are dependent on a body's shape and internal density structure. If a body's exterior figure is well known, the harmonics place strong constraints on possible internal density structures (e.g., B. C. N. Proudfoot et al. 2024a).

In this work, we present a comprehensive orbital analysis of the Quaoar–Weywot system. With nearly two decades of astrometric data, we use an advanced non-Keplerian orbit fitting scheme to better understand Quaoar's shape and interior and the dynamical environment of its ring system. In Section 2, we present new observations of Quaoar–Weywot and reanalyze archival observations. Then, in Section 3, we describe the different orbital models we use to fit our data, the results of which are presented in Section 4. We further describe the implications for Quaoar's shape and interior in Section 5 and for the albedo distribution across Quaoar's

surface in Section 6. We then examine Quaoar's ring dynamics in detail in Section 7 and finally conclude in Section 8.

2. Observations

Based on orbit fits available in the literature and updated online, past works have found significantly different orbital configurations for Weywot, even with similar datasets, presenting significant disagreements on the period and eccentricity (W. C. Fraser & M. E. Brown 2010; F. Vachier et al. 2012; W. C. Fraser et al. 2013; B. Morgado et al. 2023). Motivated by these contradictory conclusions, we have reanalyzed all past HST observations and combined them with a set of 10 new observations since 2019.

2.1. Reanalysis of Archival Observations

Between 2006 and 2008, five epochs of observations were taken by HST using both the Advanced Camera for Surveys High Resolution Channel (ACS/HRC) and the Wide Field and Planetary Camera 2 (WFPC2). An earlier analysis of this dataset (W. C. Fraser & M. E. Brown 2010) reported an eccentric orbit for Weywot. Using the ACS/HRC and WFPC2 pipelines developed to derive relative astrometry from HST images for other binary systems (e.g., W. Grundy et al. 2008, 2009), we reextracted the astrometry, obtaining positions that differ by up to 100 mas from the originally published values. Differences of this magnitude can have a substantial effect on the derived orbital solution.

Although our techniques have significant heritage and have been widely validated on many different TNO binaries (W. Grundy et al. 2019b and references therein), a selection of one pipeline over another would be ad hoc. Given the abundance of data, however, we can explicitly test which pipeline more closely matches the orbit derived with later epochs of data using a simple cross-validation test. In this, we produce an orbit fit for Weywot with each discrepant dataset and compare the fit quality. We find that the typical residuals are about an order of magnitude smaller when using our reduction, so we adopt it for the remainder of the analysis.

---

[5] Throughout this paper, to simplify discussion and provide a comparison to the literature, we assume that Quaoar's reference radius is 549 km, the volume equivalent radius found in a recent study (G. Margoti 2024).

Table 1
Observed Astrometric Positions of Weywot

Julian Date	Date	Telescope/Instrument	$\Delta\alpha\cos\delta$ (arcsec)	$\Delta\delta$ (arcsec)	$\sigma_{\Delta\alpha\cos\delta}$ (arcsec)	$\sigma_{\Delta\delta}$ (arcsec)
2453781.39621	2006/02/14	HST/ACS-HRC	+0.32879	−0.13111	0.00797	0.00253
2454179.14096	2007/03/19	HST/WFPC2	+0.31771	−0.12884	0.00188	0.00264
2454535.70523	2008/03/10	HST/WFPC2	−0.39224	−0.02512	0.00396	0.00363
2454540.56322	2008/03/15	HST/WFPC2	+0.40824	−0.07205	0.00371	0.00144
2454546.18613	2008/03/20	HST/WFPC2	−0.36223	+0.12295	0.00332	0.00370
2455719.82856	2011/06/07	Keck/NIRC2	+0.17000	−0.16000	0.01000	0.01000
2455719.89737	2011/06/07	Keck/NIRC2	+0.18000	−0.16000	0.01000	0.01000
2455719.95760	2011/06/07	Keck/NIRC2	+0.19000	−0.17000	0.01000	0.01000
2455720.01759	2011/06/07	Keck/NIRC2	+0.20000	−0.16000	0.01000	0.01000
2458700.22561	2019/08/04	Occultation	−0.41809	−0.06536	0.00396	0.00446
2459741.88464	2022/06/11	Occultation	−0.21770	+0.12770	0.00350	0.00310
2460091.16189	2023/05/26	Occultation	−0.38953	+0.03468	0.00396	0.00446
2460108.25987	2023/06/12	HST/WFC3	+0.13864	−0.13783	0.00233	0.00281
2460117.82816	2023/06/22	Occultation	−0.39599	−0.11332	0.00300	0.00300
2460452.27196	2024/05/21	HST/WFC3	−0.42830	−0.01869	0.00136	0.00100
2460484.13879	2024/06/22	HST/WFC3	+0.42755	+0.08743	0.00100	0.00100
2460764.49131	2025/03/29	HST/WFC3	−0.36510	−0.12864	0.00100	0.00127
2460770.71983	2025/04/05	HST/WFC3	+0.36846	+0.13664	0.00173	0.00100

Note. x and y correspond to R.A. and decl., respectively. Uncertainties on Δx, y have noise floors of 1 mas and 3 mas for telescope and occultation-derived observations, respectively.

In addition to the six HST detections of Weywot in this reanalyzed dataset, two additional archival observations did not detect Weywot due to its proximity to Quaoar. In principle, nondetections can be used to constrain Weywot's orbit, but doing so effectively requires a detailed analysis of the detection characteristics of the instruments used. Since the constraints placed would be relatively uninformative, especially in light of our extensive dataset, we elect to ignore these nondetections.

2.2. New Observations

Since 2023, six new epochs of HST observations have been acquired of Quaoar–Weywot using the Wide Field Camera 3 (WFC3). These observations were taken as part of HST programs 17315 and 17417. Point-spread function (PSF) fitting of each image with TinyTim (J. E. Krist et al. 2011) model PSFs was completed using the same methods as those used for the archival reanalysis. This method has been extensively validated for WFC3 observations across a variety of TNO binary observations (W. Grundy et al. 2015, 2019a). We conservatively place a 1 mas noise floor on the astrometry to account for any systematic errors in the astrometric reduction (i.e., time-variable distortion of the WFC3 field, uncertainties in pixel scale, etc.). Of the six epochs of WFC3 data, five were able to have astrometry extracted, with the one remaining epoch having an unluckily oriented PSF relative to Weywot that prevented high-quality PSF fitting.

In addition to WFC3 observations, since 2019, Weywot has been detected in four separate stellar occultations (M. Kretlow 2019; E. Fernandez-Valenzuela et al. 2023; F. Braga-Ribas et al. 2025). Although a Weywot detection alone does not necessarily provide relative position information, Quaoar's ephemeris is well known enough that the on-sky offset can be derived. We use the derived relative astrometry for the first three occultations based on circular limb fitting in F. Braga-Ribas et al. (2025). In that work, they derive a

"northern" and "southern" solution, which we average into a single data point. For the last occultation, we use the derived position of Weywot from E. Fernandez-Valenzuela (2025, in preparation), which performed an elliptical limb fit to derive Weywot's position.

For occultation-derived astrometry, various modeling choices can slightly influence the measured position of Weywot, like limb shape, timing errors, and many others. To account for these systematic effects, we place a 3 mas noise floor on all occultation-derived astrometry, approximately half the angular diameter of Weywot.

Our entire astrometric dataset is shown in Table 1. All HST data used in this paper, including the reanalyzed archival data, was retrieved from the Mikulski Archive for Space Telescopes at the Space Telescope Science Institute. The complete set of observations analyzed can be accessed via doi: 10.17909/ex7s-3w78.

3. Orbit Models

In this work, we fit the entire catalog of astrometric data using `MultiMoon`, an orbit fitter designed to work with TNO binaries (D. Ragozzine et al. 2024). `MultiMoon` treats the orbit fitting as a Bayesian parameter inference problem and uses a Markov Chain Monte Carlo (MCMC) approach. The MCMC sampler is built around `emcee`(D. Foreman-Mackey et al. 2019), a popular out-of-the-box ensemble MCMC sampler. `MultiMoon` is able to complete both Keplerian and non-Keplerian fits, accounting for the nonspherical shape of Quaoar's gravitational field. In this work, we complete a series of Keplerian and non-Keplerian orbit fits, allowing us to infer the orbital properties of Weywot and constrain the shape and spin axis of Quaoar. For further details on how `Multi-Moon` works and is used, see B. C. N. Proudfoot et al. (2024b) and D. Ragozzine et al. (2024).

Our initial orbit fitting was focused on finding a Keplerian orbit fit. Under a Keplerian orbit framework, seven free

parameters fully describe the orbit of Weywot (system mass, semimajor axis, eccentricity, inclination, and three orbit orientation angles). Our fits allow all seven parameters to vary freely. Orbit fits were run similar to past uses of `MultiMoon`'s Keplerian orbit fitter; for more details, see B. C. N. Proudfoot et al. (2024b).

Based on this set of initial Keplerian orbits fits, we found a relatively poor fit quality ($\chi^2 = 63.5$, with 29 degrees of freedom), motivating the use of a more complex orbit model. We tested several different orbit models, including non-Keplerian models, models with offsets between Quaoar's center of body (COB) and center of light (COL), and models using an outlier marginalization likelihood function (see B. C. N. Proudfoot et al. 2024a for more details). We also tested combinations of these models, finding that the best model to describe our data was a non-Keplerian model with center-of-body–center-of-light (COB-COL) offsets. Typically, model comparison requires the use of comparative metrics (such as Bayes factors, the Bayesian information criterion, etc.); however, since our models are all subsets of each other (e.g., a model with no offsets is equivalent to the offset model where the offsets are set to zero), comparison between models is vastly simplified. We find that including COB-COL offsets is strongly justified when comparing two models with and without COB-COL offsets. The fit with COB-COL offsets produces $\chi^2 = 17.3$ (0.75 per degree of freedom), while the fit without COB-COL produces $\chi^2 = 44.5$ (2.42 per degree of freedom), giving a likelihood ratio test statistic of 1.2×10^{-6} (see Section 4 of B. C. N. Proudfoot et al. 2024b). Both the improvement in χ^2 per degree of freedom and the likelihood ratio test indicate a strong preference for the COB-COL model.

The orbit model for the fits we describe here has 13 free parameters describing Quaoar and Weywot's individual masses, Weywot's six orbital elements, Quaoar's J_2 and spin pole direction, and two constant offsets between Quaoar's COB and COL in ecliptic latitude and longitude (discussed further below). Non-Keplerian effects were implemented using `MultiMoon`'s standard non-Keplerian fitting module, as described in previous work. We also input Quaoar's spin period of $\sim$17.752 hr (C. Kiss et al. 2024). The spin period controls Quaoar's axial precession period caused by Weywot's gravitational influence, which is expected to be minimal given Weywot's (presumably) small mass. Our testing in past works shows that the spin period of the primary only has a minor contribution to the overall dynamics, especially with large primary–secondary size differences (B. C. N. Proudfoot et al. 2024b).

Our orbit fits neglect C_{22} and all other higher-order harmonics. C_{22} can be safely ignored as its influence is only relevant when the spin–orbit period ratio is close to unity (i.e., near the corotation radius) or near low-order SORs (B. Proudfoot & D. Ragozzine 2021). While Quaoar has higher-order gravitational harmonics that may affect the rings, the strength of the higher-order harmonics falls off at r^{-3} (or greater). At Weywot's distance, they are expected to make only minor contributions to Weywot's dynamics.

Initial walker positions for all parameters were chosen based on high-likelihood regions identified in preliminary fits. Our orbit fits were run with 960 walkers for 10,000 burn-in steps, 5000 postpruning burn-in steps, and 25,000 sampling steps. Convergence was assessed based on autocorrelation times, as

well as the smoothness of joint and marginal posterior distributions.

3.1. COB-COL Offsets

COL-COB offsets, while described in the Appendix of B. C. N. Proudfoot et al. (2024b), have never been fully explored within `MultiMoon`. Orbit fitting for Pluto and Charon made significant use of COB-COL offsets, as both Pluto and Charon have large albedo features that create systematic, time-varying effects in Pluto–Charon astrometry. Surprisingly, COB-COL offsets can not only provide a time-variable signal but can also cause a systematic offset in relative astrometry. This effect was fully modeled for Pluto and Charon using surface maps derived from resolved HST observations, as well as mutual events (M. W. Buie et al. 1992; E. F. Young et al. 1999). Unfortunately, no such surface maps of Quaoar are available, forcing us to approximate any COB-COL effects.

Although Quaoar's true COB-COL offset likely varies in time as a result of rotating albedo features on its surface, a constant offset represents a first-order solution that can correct for *some* of the primary effects of albedo variations. Longitude-only (confined between two lines of longitude) albedo features will provide a periodic signal over a single rotation period that provides no systematic COB-COL offset. Latitude-only (between two lines of latitude) features, on the other hand, provide a constant COB-COL offset over Quaoar's rotation period. For features with both longitudinal and latitudinal components, effects can be both periodic and systematic. However, with a *large* number of samples, COB-COL variations will tend to average into an effective constant offset, though not necessarily a perfect one, and typically with a systematically higher χ^2 than expected. Of course, this averaging assumes that our data uniformly sample across Quaoar's longitude. As we discuss in Section 6.1, our dataset may not uniformly sample longitudes, which may limit the extent of the longitudinal averaging in practice. Unfortunately, implementing a rotationally variable COB-COL is quite difficult, given the lack of a precise rotational period solution for Quaoar (compare J. Ortiz et al. 2003; C. Kiss et al. 2024; G. Margoti 2024). At this early stage, with the simplicity of implementing a constant offset, we defer a more physically realistic model to future work.

Although simplistic, this model allows for exploration of a range of features that were seen on Pluto and Charon. Charon has a $\sim$longitudinally constant dark south pole, while Pluto has a dark band of red material. Such features provide a systematic effect on $\sim$all observations, which can be accounted for with our constant COB-COL offset.

With Quaoar's motion around the Sun, its pole orientation slowly varies, which could make a constant offset a poor approximation of latitudinal albedo features. However, at Quaoar's current orbital position, a constant offset in ecliptic latitude and longitude provides an excellent approximation of the changing pole orientation (as shown in Section 4).

We note that our occultation-derived relative astrometry is referenced to Quaoar's ephemeris center, rather than the true position of Quaoar during each occultation. Quaoar's ephemeris is conditioned upon telescopic observations with similar systematic COB-COL offsets as resolved imaging. As such, we treat occultation astrometry in a similar manner to all other resolved observations when fitting COB-COL offsets. In the

Table 2
Non-Keplerian Orbit Solution for Weywot

Parameter	Symbol	Constrained Fit: $\chi^2 = 37.2$	Posterior	Unconstrained Fit: $\chi^2 = 17.3$	Posterior
Fitted Parameters		Priors		Priors	
Mass, Quaoar (10^{18} kg)	M_q	$\mathcal{U}(0, 10^6]$	$1212.27^{+5.39}_{-5.39}$	$\mathcal{U}(0, 10^6]$	$1209.35^{+5.74}_{-5.58}$
Mass, Weywot (10^{18} kg)	M_w	$\mathcal{N}(2.4, 1.2)$	$2.4^{+1.2}_{-1.1}$	$\mathcal{N}(2.4, 1.2)$	$2.5^{+1.2}_{-1.2}$
Semimajor axis (km)	a	$\mathcal{U}[500, 10^{10}]$	$13,329^{+19}_{-19}$	$\mathcal{U}[500, 10^{10}]$	$13,334^{+20}_{-20}$
Eccentricity	e	$\mathcal{U}[0, 1)$	$0.0111^{+0.0044}_{-0.0040}$	$\mathcal{U}[0, 1)$	$0.0097^{+0.0027}_{-0.0024}$
Inclination (deg)	i	$\mathcal{U}[0, 180]$	$13.62^{+0.32}_{-0.33}$	$\mathcal{U}[0, 180]$	$14.83^{+0.44}_{-0.45}$
Apsidal argument (deg)	ω	$\mathcal{U}[0, 360]$	97^{+28}_{-37}	$\mathcal{U}[0, 360]$	298^{+56}_{-47}
Nodal longitude (deg)	Ω	$\mathcal{U}[0, 360]$	$353.3^{+0.83}_{-0.85}$	$\mathcal{U}[0, 360]$	$353.07^{+1.03}_{-1.25}$
Mean anomaly (deg)	$\mathcal{M}$	$\mathcal{U}[0, 360]$	79^{+39}_{-27}	$\mathcal{U}[0, 360]$	237^{+47}_{-56}
J_2 harmonic, Quaoar	J_2	$\mathcal{U}[0, 10]$	$0.018^{+0.009}_{-0.008}$	$\mathcal{U}[0, 10]$	$0.379^{+0.160}_{-0.191}$
Axis obliquity, Quaoar (deg)	$i_{\rm sp}$	$\mathcal{N}(12.6, 3.0)$	$16.53^{+1.93}_{-1.78}$	$\mathcal{U}[0, 180]$	$14.72^{+0.34}_{-0.28}$
Axis precession, Quaoar (deg)	$\Omega_{\rm sp}$	$\mathcal{N}(331.46, 3.0)$	$332.84^{+3.06}_{-3.03}$	$\mathcal{U}[0, 360]$	$353.48^{+0.78}_{-1.08}$
COL longitude offset (mas)	$\Delta x_{\rm col}$	$\mathcal{U}[-20, 20]$	$0.3^{+3.0}_{-2.9}$	$\mathcal{U}[-20, 20]$	$-0.8^{+3.0}_{-2.4}$
COL latitude offset (mas)	$\Delta y_{\rm col}$	$\mathcal{U}[-20, 20]$	$5.5^{+1.4}_{-1.4}$	$\mathcal{U}[-20, 20]$	$4.8^{+0.9}_{-0.9}$
Derived Parameters		Priors		Priors	
Keplerian orbital period (days)	$P_{\rm orb}$	⋯	$12.42727^{+0.00003}_{-0.00003}$	⋯	$12.42718^{+0.00024}_{-0.00009}$
Quaoar-centric inclination (deg)	ε	⋯	$6.13^{+1.35}_{-1.06}$	⋯	$0.41^{+0.32}_{-0.21}$
Orbit pole R.A. (deg)	α_w	⋯	$267.38^{+0.33}_{-0.32}$	⋯	$267.15^{+0.44}_{-0.52}$
Orbit pole decl. (deg)	δ_w	⋯	$53.00^{+0.33}_{-0.32}$	⋯	$51.80^{+0.45}_{-0.43}$
Mean motion (deg day^{-1})	n	⋯	$28.9586^{+0.0006}_{-0.0006}$	⋯	$28.93^{+0.01}_{-0.01}$
Apsidal precession rate (deg yr^{-1})	ϖ	⋯	$0.48^{+0.24}_{-0.21}$	⋯	$10.19^{+4.29}_{-5.13}$
Nodal precession rate (deg yr^{-1})	$\dot{\Omega}$	⋯	$-0.49^{+0.21}_{-0.24}$	⋯	$-10.19^{+5.13}_{-4.29}$

Note. Reported values represent the median value and uncertainties and are based on 16th and 84th percentile values. Priors are either uniform ($\mathcal{U}$) with upper and lower bounds listed or normally distributed ($\mathcal{N}$) with mean and scale listed. All fitted angles are relative to the J2000 ecliptic plane on Quaoar-centric JD 2454000.0 (2006 September 21 12:00 UT), except for R.A. and decl. values, which are referenced to the J2000 equatorial coordinate system. The assumed c-axis for Quaoar is 545 km, and the spin period is 17.752 hr (C. Kiss et al. 2024), although realistic variation of these values produces no meaningful change to the fit. To transform to J_2 from the more physically meaningful $J_2 R^2$, we use a volumetric radius of 549 km.

future, an entire dataset made of double occultations (where both Quaoar and Weywot are detected) could obviate the need for COB-COL offsets.

3.2. Priors

Priors for most parameters were chosen to be uninformative, mostly limiting the parameters to physical/realistic values. For Weywot's mass, which is relatively unconstrained by our orbit model, we placed a Gaussian prior with a mean of 2.4×10^{18} kg and a standard deviation of 1.2×10^{18} kg, roughly corresponding to the mass expected with a diameter of 165 km (E. Fernández-Valenzuela 2025, in preparation) and density between 500 and 1500 kg m^{-3}. Since Weywot's mass is very weakly correlated with Quaoar's J_2, this ensures the most physically realistic model, which is important when later characterizing the dynamics of the ring system.

Quaoar's spin pole direction is constrained by the pole orientation of its two rings. As collisional systems, rings tend to damp to the local Laplace plane (i.e., the plane that minimizes perturbations), which is usually close to a body's equatorial plane. Based on the precession rates from Quaoar's J_2 and Weywot, the Laplace plane should be $\lesssim 0.^\circ 5$ inclined from Quaoar's equatorial plane (assuming a large range of Weywot densities). Thus, we can assume that Quaoar's pole orientation is close to that of the ring plane. Recent work combining all detections of Quaoar's rings—including new detections with JWST—have enabled precise measurement of Quaoar's ring pole (B. Proudfoot et al. 2025). This work is the first to use a self-consistent model of the rings that accounts for

their changing geometry since their first detection in 2018. We use those measurements as a Gaussian prior, although we inflate the uncertainties to 3°. This accounts for any systematic effects in the ring modeling procedures. For example, Q1R is expected to have a fairly high eccentricity (A. Rodríguez et al. 2023), which can bias measurements of pole direction when modeling the rings as circular. Likewise, any warps or bending waves (see Section 7) may also bias ring pole determinations. For comparison, we also run a fit without any priors on Quaoar's pole orientation. We refer to these two different fits as the constrained fit and the unconstrained fit throughout the rest of this paper.[6]

4. Orbit Fitting Results

The results of our orbit fits are presented in Table 2 alongside a variety of derived parameters. We also show corner plots of the posterior distributions in Figures 2 and 3. These orbit fits represent the most detailed exploration of Weywot's orbit to date.

Comparison between the orbit fits shows many fundamental differences. Most importantly, the fit quality of the unconstrained orbit fits is substantially better, with a best-fit χ^2 per degree of freedom of 0.80 compared to 1.62 for the constrained fit. This difference in fit quality is primarily a function of Quaoar's J_2 and pole direction. This can be further

---

[6] We note that the COB-COL likelihood ratio test for the constrained fit produces a likelihood ratio of 8.3×10^{-6}, still indicating a strong preference for a model with the COB-COL offset included.
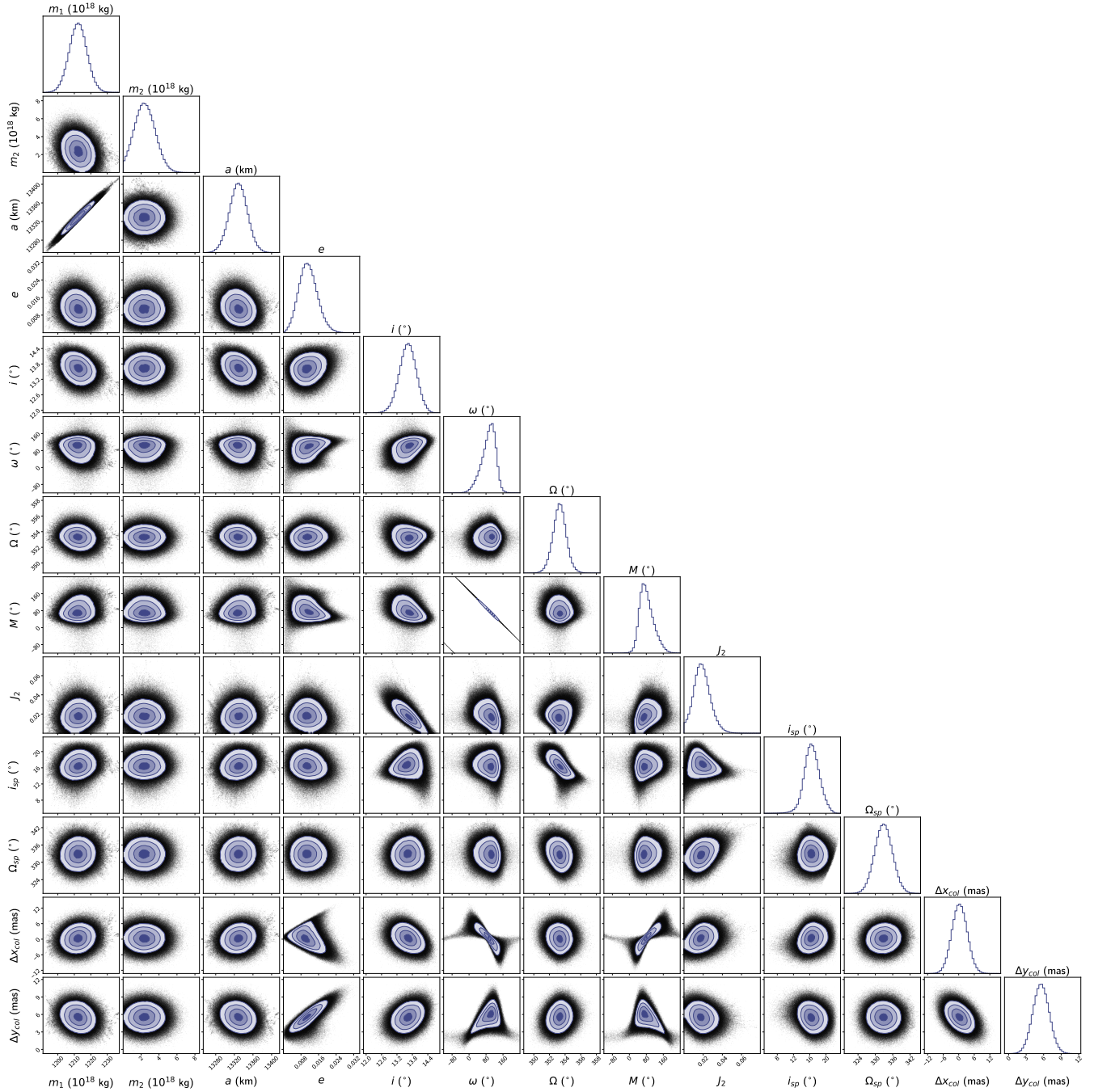
Figure 2. A corner plot showing the posterior distribution from our constrained orbit fit. Along the diagonal are the marginal (1D) posterior distributions for each parameter alongside the 2D joint posterior distributions for each pair of parameters. Contours on the joint distributions show the 1σ, 2σ, and 3σ confidence regions, and black points correspond to individual samples from the MCMC chain.

simplified as a correlation between fit quality, Quaoar's J_2, and Weywot's inclination (which simplifies the complex dependency between orbit and spin orientation angles). Fit quality is relatively high at low Weywot inclination, with a broad range of allowable values for Quaoar's J_2. Conversely, at high Weywot inclination ($\gtrsim 1°$), fit quality is much lower but permits a small range of nonzero values for Quaoar's J_2. We show this correlation in Figure 4.

One possible explanation of the large difference in fit quality between the orbit fits is systematic errors induced by time-varying COB-COL offsets, which are overfitted by the unconstrained model. As an example, consider the astrometry

of Weywot when Quaoar has a time-varying COB-COL offset. The motion of the COL will be some complicated periodic function set by the albedo distribution, Quaoar's rotation period, Quaoar and Earth's heliocentric motion, the telescope filter (since the albedo distribution can differ at varying wavelengths), and a variety of other factors. With enough observations, the offset in the direction perpendicular to the pole position angle will tend to average out, given Quaoar's nonsynchronous rotation. But given just a handful of observations that are sparsely sampled, the effects of this COB-COL wobble (when unaccounted for) will reduce the fit quality. Our new HST observations are quite precise, with
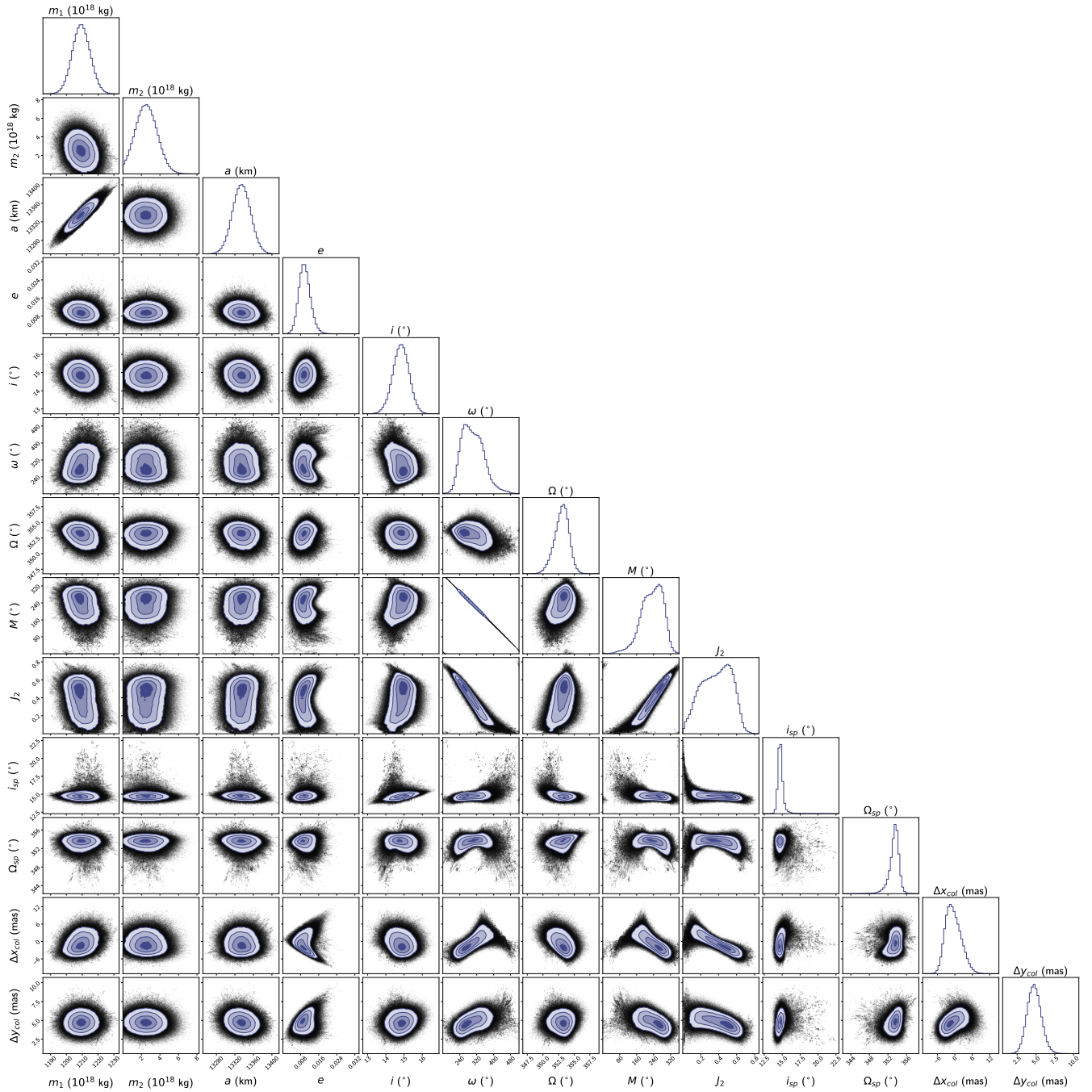
Figure 3. Similar to Figure 2 but for the unconstrained orbit fit.

uncertainties on the order of 1 mas. With an angular diameter of Quaoar of ∼40 mas, even small albedo variations could induce significant systematics. Rapid precession on a nearly circular/equatorial orbit (as seen in our unconstrained fit) would induce a similar wobbling motion, which could coincidentally produce a better fit to the astrometry.

The implied J_2 in our unconstrained orbit fit is likely to be unrealistically high, unless undiscovered moons remain undetected within Weywot's orbit or Quaoar's ring system is unexpectedly massive. Likewise, the pole orientation of Quaoar in these fits is very different than that implied by the orientation of Quaoar's ring system, with a ∼5° inclination. In comparison, the constrained orbit fit is roughly consistent with shape/interior models for a differentiated Quaoar (see

Section 5 for more exploration of this). Given that the constrained fits seem to be more physically realistic in terms of Quaoar's J_2 and pole orientation, we believe the constrained model likely provides a more accurate representation of the Quaoar–Weywot system, even with the lower fit quality.

Other than the differences in Quaoar's J_2—and the corresponding changes in orbit/spin orientation angles—our two orbit fits are remarkably consistent with one another. Both fits provide a determination of Quaoar's mass (when using the Weywot mass prior), with only 0.5% uncertainties in both orbit fits. Likewise, the orbit fits provide precise determinations of Weywot's semimajor axis, which is important for understanding the location of Weywot's 6:1 MMR near the outer ring. Combined, the mass and semimajor
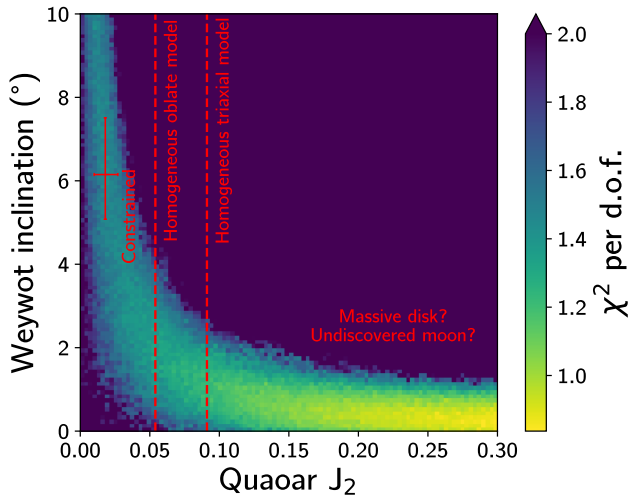
Figure 4. Orbit fit quality (χ^2 per degree of freedom) as a function of Quaoar's J_2 and Weywot's inclination (with respect to Quaoar's equatorial plane). Red dashed lines show the values expected from the undifferentiated oblate and triaxial shape models. The red cross shows the J_2 and inclination value measured in the constrained orbit fit. We note that the best fit quality is at $J_2 \sim 0.4$, but we limit the range of J_2 displayed to better show the fit quality at more realistic values of Quaoar's J_2. For reference, the p-value of $\chi^2_{pdf} = 1$ (1.8) is 0.46 (0.01).

axis determinations allow for an ultraprecise measurement of Weywot's orbit period, with an uncertainty of <20 s and $10\times$ more precise in the constrained fit.

Both our orbit fits also show a small eccentricity, differing from most previous orbit fits in the literature. This is largely the result of our astrometric reanalysis described in Section 2.1. We consistently find $e < 0.02$, even without the inclusion of any data from 2019 or later. Recently published work using our reanalyzed dataset—but not our new HST data—shows a similarly low eccentricity, emphasizing the importance of the reanalysis (F. Braga-Ribas et al. 2025).

In our fits, e is also strongly correlated with the COB-COL offsets. To first order, a circular orbit with a small COB-COL offset appears as a slightly eccentric orbit, so seeing such a correlation is not unusual (e.g., M. W. Buie et al. 2012). More realistic COB-COL offsets should further refine Weywot's actual eccentricity, but here, we place an upper limit of $e < 0.02$. Weywot's eccentricity is important for understanding the dynamics of Quaoar's rings, and this upper limit limits their dynamical strength.

One of the most interesting aspects of our orbit fits is the strong preference for nonzero COB-COL offsets. We find strong evidence for COB-COL offsets, with both orbit fits measuring a nonzero average offset at $\gtrsim 4\sigma$ confidence. Preliminary Keplerian orbit fits also found nonzero offsets at $\sim 4.5\sigma$ confidence. As discussed previously, these offsets are not physically realistic by construction; however, as can be seen in Figure 5, the constant offset (in ecliptic latitude and longitude) tracks similar positions on Quaoar's surface throughout our observational baseline. This coincidentally allows the constant COB-COL offset to provide a physically meaningful model, validating our method of implementation.

In both fits (and preliminary Keplerian fits), the offset implied is roughly aligned with the projected pole direction of Quaoar, which is consistent with significant latitudinal albedo variations across Quaoar's surface. Although this could occur randomly by chance ($\sim 5\%$), this alignment is suggestive that
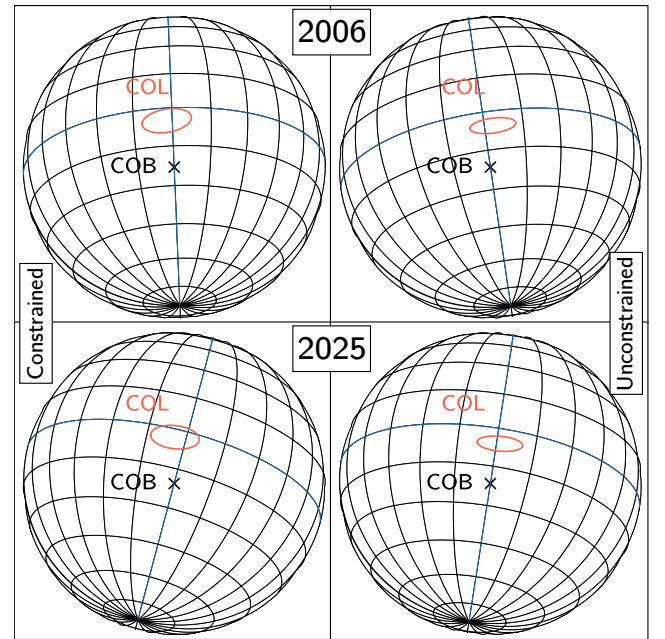

Figure 5. The COL-COB offsets implied by our constrained (left) and unconstrained (right) orbit fits. The COL is shown as a red ellipse (based on the orbit fit posterior) and the COB is marked with a black cross. Quaoar is shown as a sphere with an angular diameter of 36 mas. The equator and subobserver longitude are shown with blue lines. Over our observational baseline, a constant offset in ecliptic latitude and longitude is a good approximation of a COB-COL offset caused by longitudinal albedo features.

the COB-COL offsets in our models represent real albedo features. Interestingly, for both our orbit fits, the implied COL (shown as a red ellipse in Figure 5) is nearly coincident with Quaoar's equator. This could provide a hint about the albedo distribution of Quaoar. In Section 6, we discuss this further.

Given the long observational baseline of our data, we are able to fully determine the orbital plane of Weywot. With a small dataset, orbit fitting is generally not able to fully determine a satellite's orbital plane, leaving two ambiguous solutions that are mirror images of one another. Mirror solutions have never been formally ruled out in the literature, making it unclear if mirror solutions have ever been formally excluded. During our early Keplerian orbit fits, we found that the mirror solutions provided a much worse fit to the data and could be excluded at $>50\sigma$ confidence.

To facilitate future observations of Weywot, predictions of occultations, and a variety of other scientific investigations, we include an ephemeris of Weywot referenced to Quaoar's COL. This ephemeris—spanning from 2005 until 2035—is generated by taking 500 random posterior samples from the constrained-fit MCMC chain. The first 10 rows of this ephemeris are displayed in Table 3, with the rest of the ephemeris available as a machine-readable table.

5. Quaoar's J_2 and Interior

5.1. Shape Models

As guides for our interpretation of Quaoar's J_2, we consider two recently published shape models for Quaoar. The first shape model was developed to fit the visible and thermal light curves of Quaoar, as well as its overall thermal emission (C. Kiss et al. 2024). The thermophysical study, assuming a constant global albedo, predicted axis ratios of $a/b = 1.19$ and

Table 3
System Ephemeris

Julian Date	Date	$\Delta\alpha\cos\delta$ (arcsec)	$\sigma_{\Delta\alpha\cos\delta}$ (arcsec)	$\Delta\delta$ (arcsec)	$\sigma_{\Delta\delta}$ (arcsec)	r (arcsec)	σ_r (arcsec)
2453371.5	2005-01-01 0:00:00	0.36355	0.00124	−0.11581	0.00137	0.38152	0.00129
2453371.75	2005-01-01 6:00:00	0.38515	0.00109	−0.10207	0.00128	0.39845	0.00111
2453372	2005-01-01 12:00:00	0.40074	0.00100	−0.08664	0.00124	0.41003	0.00100
2453372.25	2005-01-01 18:00:00	0.41003	0.00098	−0.06977	0.00124	0.41591	0.00098
2453372.5	2005-01-02 0:00:00	0.41287	0.00104	−0.05170	0.00129	0.41610	0.00105
2453372.75	2005-01-02 6:00:00	0.40918	0.00118	−0.03272	0.00139	0.41053	0.00119
2453373	2005-01-02 12:00:00	0.39901	0.00140	−0.01314	0.00150	0.39926	0.00141
2453373.25	2005-01-02 18:00:00	0.38248	0.00168	+0.00674	0.00164	0.38261	0.00167
2453373.5	2005-01-03 0:00:00	0.35985	0.00200	+0.02660	0.00178	0.36089	0.00197
2453373.75	2005-01-03 6:00:00	0.33144	0.00233	+0.04612	0.00193	0.33472	0.00229

Note. The predicted R.A. and decl. positions of Weywot—referenced to Quaoar's COL—from 2005 through 2035. Predicted positions, separations, and uncertainties are taken from a sample of 500 random posterior draws from the constrained orbit fit.

(This table is available in its entirety in machine-readable form in the online article.)

$b/c = 1.16$, with a range of possible volumetric radii. We assume a volumetric radius of 549 km (to simplify the comparison between shape models), which gives $a = 648$ km, $b = 544$ km, and $c = 469$ km. We refer to this as the light-curve shape model.

In contrast, G. Margoti (2024) used 62 positive occultation chords over 20 different occultations to derive the 3D shape of Quaoar. This method allows a better determination of the shape, without requiring any assumptions about Quaoar's albedo, giving $a = 583.3 \pm 2.6$ km, $b = 555.3 \pm 1.0$ km, and $c = 510.0 \pm 1.0$ km and a volumetric radius of 548.8 ± 1.1 km. We refer to this as the occultation shape model.

With both of these shape models, we can derive Quaoar's expected J_2 assuming various internal density structures. With a homogeneous interior (i.e., undifferentiated), J_2 is a function of the semiaxes a, b, and c, where

$$J_2 = \frac{1}{10R^2}(a^2 + b^2 - 2c^2) \qquad (2)$$

(C. F. Yoder 1995), giving $J_2 = 0.092$ and $J_2 = 0.043$ for the light-curve and occultation models, respectively. Quaoar, however, as a large TNO, has likely sustained high temperatures in its interior, allowing at least partial differentiation. Its large density hints that gravitational compaction, or even melting, could have eliminated internal pore space (C. Bierson & F. Nimmo 2019). This is further evidenced by light hydrocarbons on its surface, which could be derived from internal geochemical processes (J. Emery et al. 2024).

5.2. How Does Differentiation Change J₂?

To account for differentiation, we can instead consider a two-layer density model with a spherical rocky core at its center surrounded by a partially (or totally) differentiated shell. Selecting a core radius and density, we can calculate a core volume and mass, which sets the shell shape, volume, and density (based on the shape model and mass given by our orbit fits). The gravitational harmonics of a given shape (with mass, M) are determined by its principal moments of inertia. J_2 is given by

$$J_2 = \frac{C - \frac{1}{2}(B + A)}{MR^2} \qquad (3)$$

(C. F. Yoder 1995), where A, B, and C are the principal moments of inertia around the a, b, and c axes. Using the shape and density of the core and shell, we can calculate J_2 solely as a function of the shape model, core density, and core radius. We show these relationships in Figure 6, where the far left models correspond to an undifferentiated body and the far right models correspond to a fully differentiated body with a shell density of pure water ice (920 kg m^{-3}). We select a range of core densities based on the densities of hydrated and dehydrated rock, 2600 kg m^{-3} and 3800 kg m^{-3}, respectively (E. Dunham et al. 2019; J. L. Noviello et al. 2022). Assuming a spherical core places a lower bound on J_2 when considering differentiation, since Quaoar's core is likely not spherical, especially given Quaoar's external shape.

To more accurately consider the core shape, we also complete the same analysis as above but instead model the core with the same axis ratios as the external shape. We show this sequence of models in the right panel of Figure 6. Since a rocky core is more dense than the external shell, the core is likely to be somewhat less oblate/prolate than the external figure. Hence, these models are probably more of an overestimate of J_2, which we consider as a rough upper bound.

We note that these two-layer models are not fully self-consistent models that satisfy hydrostatic equilibrium, although they serve as a useful guide for understanding how differentiation affects J_2. In the future, self-consistent hydrostatic equilibrium models, like those implemented in `kyushu` (E. Dunham et al. 2019), can be used to jointly interpret Quaoar's J_2 and external figure.

5.3. Quaoar's Interior from Orbit Fits

With realistic estimates/bounds on possible J_2 values, we can compare with the results of our orbit fitting to glean insights into the interior of Quaoar. Focusing on the constrained orbit fit, we find that the measured J_2 is consistent with the differentiated occultation model (when taking the
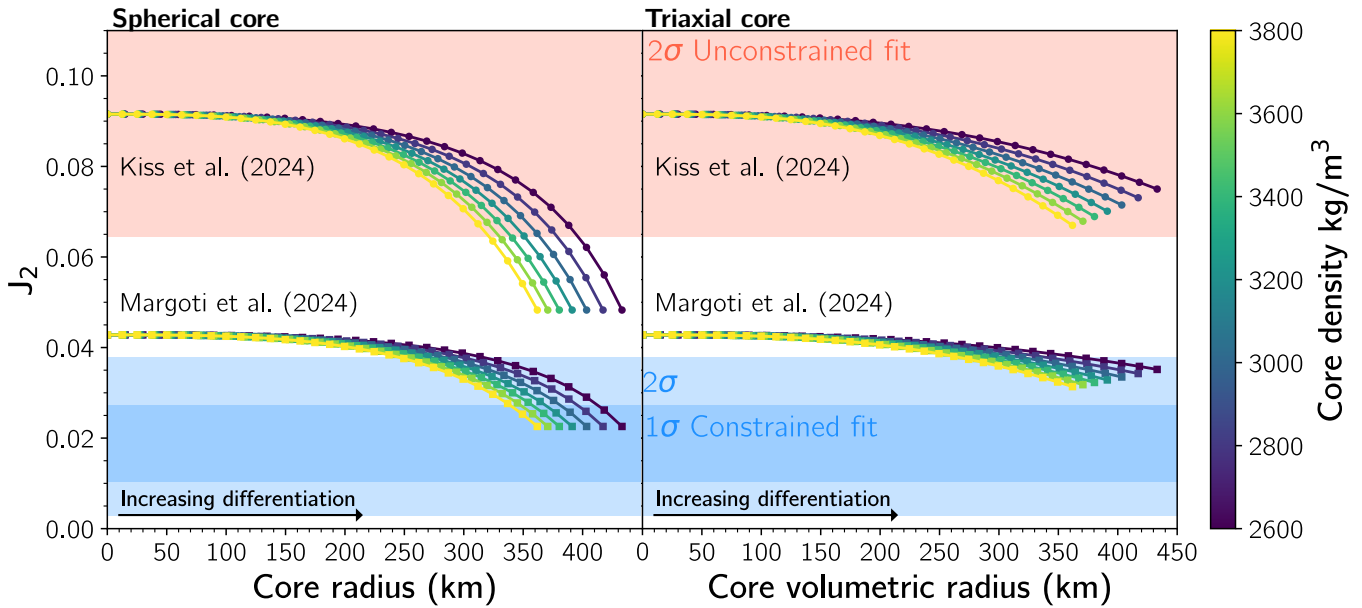
Figure 6. J_2 values for Quaoar as a function of core size and core density assuming a two-layer interior structure model with spherical cores (left) and triaxial cores (right). The two-layer interior model consists of a rocky core (with chosen core density) surrounded by a partially differentiated shell of mixed ice and rock. Points at core radii of 0 km correspond to an undifferentiated model, and the maximum core radii correspond to a fully differentiated body with a shell density of water ice (920 kg m^{-3}). Core densities are chosen to bound likely core densities of TNOs with 2600 kg m^{-3} corresponding to hydrated rock and 3800 kg m^{-3} corresponding to dehydrated rock.

average of the spherical and triaxial core models) but inconsistent with the undifferentiated model. It is also wholly inconsistent with the light-curve model, even when considering differentiation. Looking to the unconstrained fit, both shape models provide poor fits, although the undifferentiated light-curve shape model fits the J_2 posterior at $\sim 2\sigma$.

Assuming that the constrained fit is a better description of Weywot's orbit, we suggest that Quaoar is differentiated and has a shape consistent with the occultation-derived shape model. As this model predicts a lower-amplitude light curve than observed (G. Margoti 2024), we further suggest that Quaoar's light curve is shaped by albedo features. Based on our measurement of Quaoar's mass, the occultation shape model produces a density of 1751 ± 13 kg m^{-3}. We note, however, at such precision, systematics from other effects (such as topography, slight nontriaxiality, etc.) could be important for a precise measurement of Quaoar's bulk density.

During our preliminary fits, we also explored orbit models with robust outlier detection methods implemented (as in B. C. N. Proudfoot et al. 2024a). These models provide a useful way to examine whether our results could be biased by potential outliers or underestimated errors. Those orbit fits show nearly equivalent orbit solutions, although they can only place an upper limit of $J_2 < 0.026$ (0.042) at 1σ (2σ) confidence, fairly similar to the $1/2\sigma$ limits in the constrained fit. This suggests that our inferences are robust to possible outliers or data quality issues.

We reemphasize that, as seen in Figure 4, J_2 and Weywot's inclination (with respect to Quaoar's equator) are strongly correlated. Our constrained fit assumes that Quaoar's pole is aligned with the ring system and that the rings' pole orientation is well measured. Unlike Chariklo or Haumea, the orientation of Quaoar's rings has *never* been measured at a single epoch. Instead, the orientation of the rings is measured by combining detections from many epochs, which could introduce systematic errors. For example, A. Rodríguez et al. (2023) suggest that

based on width variations in Q1R, the ring is expected to have $e \gtrsim 0.036$. Such a ring would slowly precess, creating complications in combining temporally separated detections. This could easily lead to significant uncertainties in our knowledge of the ring pole. As such, fits should be updated once the ring system is better characterized. We especially encourage large occultation campaigns that could characterize the ring orientation and eccentricity at a single epoch.

5.4. Massive Disks and/or Undiscovered Satellites?

Although we do consider the constrained model to provide a better description of Weywot's dynamics, it is worth exploring the implications of the high J_2 value found in the unconstrained model. Although the unconstrained model is 2σ consistent with the triaxial model, the bulk of the posterior has much higher values for J_2. One possible reason for this would be orbiting mass between Quaoar and Weywot.

Although no definitive measurements of the mass of Quaoar's ring system have been made, we can place an upper limit on it by comparing to Haumea's and Chariklo's rings. B. Sicardy et al. (2020) suggest that Haumea's and Chariklo's ring systems likely have similar surface densities as Saturn's A ring, ~ 500–1000 kg m^{-2}. Generously assuming the same surface density, despite it being the least dense small-body ring system, we find an upper limit on the mass of Quaoar's rings of $M_r \sim 10^{16}$ kg, equivalent to an icy body with a radius of 15 km. The J_2 contribution of a ring can be derived from Equation (3), giving

$$J_2 \approx \frac{1}{2} \frac{M_r}{M_q} \left(\frac{r}{R} \right)^2, \qquad (4)$$

where r is the ring radius. This yields $J_{2,\mathrm{ring}} \sim 0.0002$, contributing almost no detectable signature when compared to our estimates of Quaoar's J_2. Evidently, Quaoar's rings contribute little to the dynamics of Weywot.

Another possibility is the presence of undetected moons between Quaoar and Weywot. Moons embedded within/near Quaoar's rings would have a maximum angular separation from Quaoar of $\sim0.''15$, which is equivalent to <4 WFC3 pixels. This separation is difficult to resolve with current telescopes, even JWST. As such, it remains possible for inner satellites to remain undiscovered around Quaoar. To explain the entirety of the J_2 measured in our unconstrained fit using Equation (4), a satellite orbiting at 5000 km would need a mass of $\sim10^{19}$, roughly equivalent to an icy body with a radius of ~140 km. Such a massive satellite could present stability issues for the ring system, unless the rings are at/near resonance with this putative moon. A system of shepherd satellites could also play a role in raising the apparent J_2 but would require $\sim$thousands of 10 km bodies to generate the same J_2 signature.

Another satellite interior to Weywot could help to explain Weywot's substantial inclination relative to the ring plane ($\sim5°$ in the unconstrained fit). Similar to Hi'iaka and Namaka, Weywot could have its inclination excited by a massive companion (D. Ragozzine & M. E. Brown 2009; B. C. N. Proudfoot et al. 2024a).

Although we encourage observations to search for additional satellites around Quaoar, we believe it is unlikely that enough orbiting mass exists around Quaoar to generate the J_2 signal that our fits imply. As such, we consider the constrained orbit fit to be the more realistic fit, especially when considering its alignment with the ring system.

6. COB-COL Offsets and Quaoar's Surface

Until now, COB-COL offsets have not been a necessary part of any orbital model for TNO binaries/satellites, with the exception of Pluto. With an angular diameter of up to 110 mas, along with drastic albedo features, Pluto's COB-COL offsets are a necessary part of any orbital model. These offsets were studied at length in the decades before the New Horizons flyby. Surface albedo maps were originally made by taking advantage of Pluto's 1985–1990 mutual event season (M. W. Buie et al. 1992) and were further supplemented by imaging of Pluto and Charon with HST's ACS instrument that could partially resolve Pluto's surface (M. W. Buie et al. 2010). Orbit fits without these albedo maps consistently generate nonzero eccentricities and large residuals (e.g., D. J. Tholen & M. W. Buie 1997). One important aspect of these COB-COL offsets is a systematic offset in the astrometry, in addition to a periodic signal phased to the rotation period. This is seen in Figure 9 of M. W. Buie et al. (2012), where orbit fits for Pluto and Charon have systematic offsets of ~7–8 mas. With measurement uncertainties of order ~1 mas (see Table 1), it quickly becomes clear that Quaoar could be significantly affected by similar issues.

In both our orbit fits, we find significant detections of COB-COL offsets. Our constrained fit shows a total COB-COL offset of 5.5 ± 1.4 mas, and our unconstrained fit shows an offset of 4.9 ± 1.0 mas, corresponding to about 170 and 150 km at Quaoar's typical distance of ~42 au. These offsets appear to be well aligned with the projected position angle of Quaoar's pole, suggesting that the offsets are modeling a real phenomenon.

Although large, plausible surface albedo features could explain these offsets. We explored a few toy models of Quaoar's albedo and found that latitudinal variations of albedo

(by a factor of a few) could explain these offsets. For example, a map where Quaoar has a bright equatorial band—putatively created by slow infalling of ring material—can have COB-COL offsets of the same magnitude and direction as our fits.

Alternatively, a dark pole with an albedo a few times smaller than the global average albedo could similarly produce offsets the size we see—akin to Charon's dark north pole. Recent JWST observations show that C_2H_6 is present on Quaoar's surface (J. Emery et al. 2024). How would C_2H_6 behave in Quaoar's surface environment? Sublimation tends to be driven by the maximum temperatures reached. For Quaoar's perihelion distance, a low albedo, low thermal inertia region at the subsolar point could reach temperatures approaching 63 K. At that temperature, the equilibrium vapor pressure of C_2H_6 is 6×10^{-11} bars (N. Fray & B. Schmitt 2009), which, according to the Hertz–Knudsen–Langmuir equation (I. Langmuir 1913), produces a sublimation rate into vacuum of 0.055 g cm^{-2} yr^{-1}, or the loss of 1 g cm^{-2} in just 18 yr. Velocities of sublimating C_2H_6 molecules will be governed by the Armand distribution (G. Armand 1977; N. Schörghofer 2022). Compared to Quaoar's escape velocity of ~540 m s^{-1}, these velocities are mostly lower, with only 0.07% of sublimating C_2H_6 molecules exceeding escape velocity. The rapid sublimation and low escape fraction suggest that C_2H_6 should migrate away from equatorial latitudes relatively quickly. Thanks to Quaoar's low obliquity, high latitudes remain much colder, so C_2H_6 will tend to accumulate there. Over time, it should be radiolytically processed into a dark, reddish, high molecular mass residue. Quaoar's current orientation allows us to see a dark south polar region, while hiding much of the north polar region, providing a systematic offset between Quaoar's COL and COB.

6.1. Possible Systematics

One issue with our detections could be incomplete longitudinal sampling of Quaoar's surface. When looking to our astrometric data (Table 1), most of our observations are relatively insensitive to the COB-COL offsets, with the offsets being 1–2 times the size of typical error bars. In contrast, our last four observations, all from WFC3 in 2024–2025, are much more sensitive to putative COB-COL shifts, with the offsets being ~4–6 times the size of the typical error bars. With observations at just four different longitudes, it may be possible that our sampling of Quaoar's surface may be incomplete. Indeed, taking the times of our last four observations and calculating their rotational phase (with a rotational period of 17.752 hr; C. Kiss et al. 2024), three of the four fall within phases from 0 to 0.1, just 10% of all possible longitudes. With this unlucky phasing, our fits may be particularly biased toward a single longitude, providing a skewed measurement of the COB-COL offset. Again comparing to COB-COL offsets for Pluto, sampling at a single phase could produce an offset as much as $\sim40\%$ higher/lower than the true mean (see Figure 18 in M. W. Buie et al. 2010). Similar issues can come from wavelength-dependent COB-COL offsets, which are again important for modeling Pluto's surface.

Another way to probe the true COB-COL offset is to consider Weywot's eccentricity. As shown in Figures 2 and 3, the COB-COL offset is strongly correlated with the fitted eccentricity. Weywot's nonzero eccentricity is interesting when considering the timescale for tidal circularization. Using the circularization timescale from P. Goldreich & S. Soter

(1966), we find that Weywot's circularization timescale is $\lesssim$10 Myr, assuming a range of values for Weywot's density and size. We can then ask, if Weywot is on a circular orbit, what is the required average COB-COL offset to explain our data? Visual inspection of the $e - \Delta x_{col}$ and $e - \Delta y_{col}$ joint posterior distributions in Figures 2 and 3 show that this occurs near 2–3 mas of total offset. This may be closer to the true COB-COL offset for Quaoar. Offsets of this size are plausible, as they are the same magnitude as those on Pluto ($\sim$5%–10% of the angular diameter). We note that even a circularized Weywot could still retain a small inclination, as the inclination damping timescales can be orders of magnitude longer than the eccentricity damping timescales (C. D. Murray & S. F. Dermott 1999).

Although we interpret our measured offsets as features on Quaoar's surface, Quaoar's ring system could also contribute to COL variations. A circular homogeneous ring orbiting Quaoar's center-of-mass (COM) would provide no net COB-COL, but Quaoar's rings are known to contain denser arcs of material that could provide a net offset. In principle, these offsets may average out over a large number of observations, but as discussed above, our dataset may not be large enough at this point in time. On the other hand, if the outer ring's arc-like structure(s) are confined within Weywot's nearby 6:1 MMR, offsets may be a function of Weywot's orbital phase, providing a systematic bias that may not fully average out. With so little known about Quaoar's rings, we leave a full accounting of their COB-COL effects to future work.

Likewise, Quaoar's triaxial shape could introduce COB-COL offsets. Although the center of the projected limb of a triaxial body is coincident with the COB, the COL of the visible hemisphere is not necessarily aligned. Depending on the surface reflectance properties, the COL could vary significantly, and may even have systematic offsets. We leave the exploration of shape-generated COB-COL offsets to future work.

Also of note are possible offsets between Quaoar's COM and its COB. Throughout this work, we assumed that Quaoar's COB and COM are coincident, but this may not be justified. For example, the Moon has a well-studied COB-COM offset. These offsets, however, will typically be very small. As implied by our low J_2 measurement, Quaoar's interior likely experienced some degree of melting, allowing hydrostatic relaxation to take place, minimizing COB-COM offsets. Offsets could later develop, possibly after freezing of Quaoar's interior, but would remain small. In any case, our model actually probes COM-COL offsets, so they are fully accounted for in our fits (assuming an averaged constant offset).

6.2. How Do COB-COL Offsets Affect Other Parameters?

With such uncertainty associated with our measurements of COB-COL offsets, how are our other results impacted? Looking to Figure 2, the constrained-fit J_2 measurement is relatively uncorrelated with the offsets, although a slightly smaller Δy_{col} implies a slightly larger value of J_2. More broadly, Δx_{col} and Δy_{col} seem to be primarily correlated with e, ω, and $\mathcal{M}$—which is unsurprising given the discussed correlation with e—while most other parameters seem to be generally un-/weakly correlated. Moving to the unconstrained fit, Δx_{col} and Δy_{col} appear to be mainly correlated with e and orbit angles, although a modest correlation with J_2 is also present. This correlation with J_2 is indirect. While J_2 and the

COB-COL offsets should not be correlated, both J_2 and the offsets are correlated with the orbit angles, indirectly making J_2 and the offsets have a correlation. Indeed, this can be seen when comparing the J_2–$\Delta x/y$ posteriors with the J_2–ω posteriors, which appear to be mirror images.

In addition to the fits we present here, we also conducted a series of orbit fits (both constrained and unconstrained) without COB-COL offsets. These fits show remarkable similarity with their COB-COL counterparts, providing nearly identical orbital periods, orbit pole orientation (i, Ω), and measurements of non-Keplerian effects. This strongly suggests that the rest of our interpretation is fairly insensitive to constant COB-COL effects.

If longitudinally variable COB-COL offsets are present, could we be confusing them for non-Keplerian motion? Given Weywot's small eccentricity, the dominant source of non-Keplerian effects will be nodal—rather than apsidal—precession. Nodal precession will primarily cause the orientation of the orbit to subtly change, which would primarily generate motion in the Δy-direction with positive/negative offsets on each side of the orbit. In contrast, longitudinal albedo variations will primarily cause Δx motion over a Quaoar rotation period. This makes it difficult to confuse nodal precession and varying COB-COL offsets, again suggesting that our results concerning Quaoar's J_2 are not significantly altered by COB-COL effects.

6.3. Moving to a Longitudinally Variable COB-COL Model

Disentangling Quaoar's COL-COB offsets from Weywot's orbital motion is difficult. The work we present here is just a first-order approximation of the effect, which could be significantly influenced by incomplete sampling of Quaoar's surface. Moving forward, more physically motivated models should be used to better determine these effects. Most importantly, a longitudinally variable COB-COL offset should be used. Given the light-curve amplitude of Quaoar, our suboptimal fit quality, and the comparison to Pluto and Charon, it is likely that detailed surface maps of Quaoar are needed to fully explain Weywot's orbital motion.

Although surface maps are likely more than a decade away, simple implementations of longitudinal variation can be used to jointly understand Weywot's orbit and Quaoar's surface. For example, a simple second-order model could use a constant offset and a few Fourier terms to replicate some of the surface albedo variations. Using techniques similar to those used for Pluto's mutual events, these could plausibly be inverted to provide crude surface maps (M. W. Buie et al. 1992). Self-consistent modeling of viewing geometry changes from Quaoar and Earth's heliocentric motion should also be included. Alternatively, spherical harmonic expansions could be used to model the longitudinal variations. Various tools have been developed in the exoplanet literature to model starspots' effects on exoplanet transit light curves that could be adapted for this problem (e.g., R. Luger et al. 2019).

Prior to the development of these models, significant work will have to be done to study Quaoar's light curve in more detail. A precise rotation period—which remains elusive for Quaoar—is perhaps the most important measurement to be input into COB-COL models. Without it, phasing all the astrometric observations will be impossible. In addition, a precise light curve can also aid in understanding the COB-
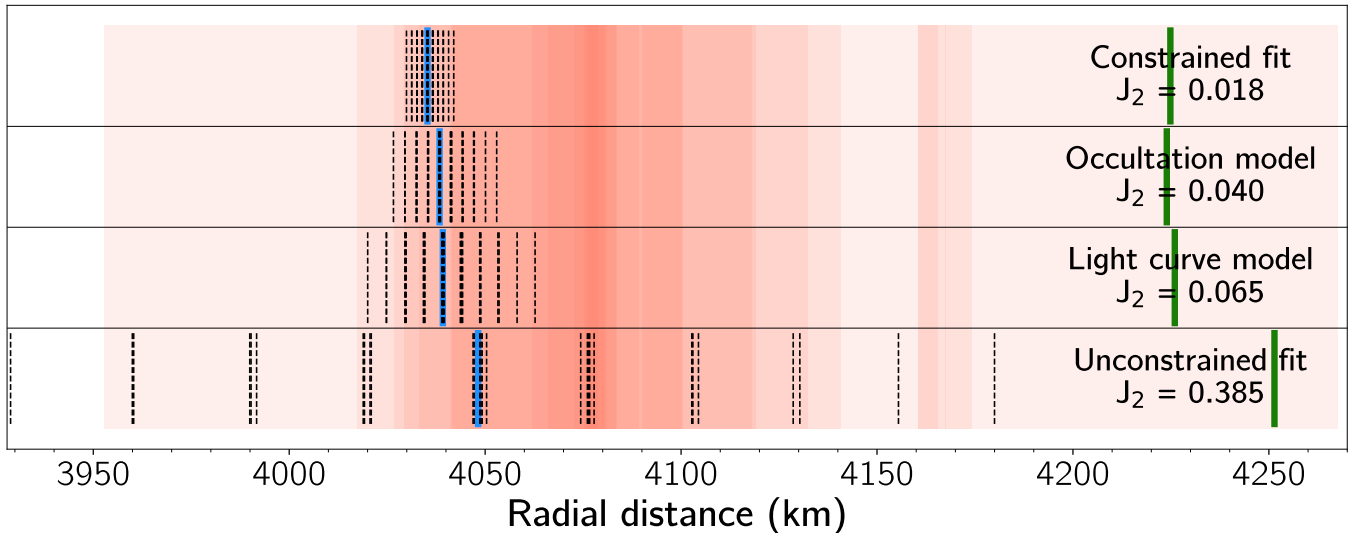
Figure 7. Resonance splitting of Weywot's 6:1 MMR based on the constrained fit, the differentiated occultation model, the differentiated light-curve model, and the unconstrained fit. The various 6:1 subresonances are shown as dashed black lines, with the nominal location of the resonance shown in blue. Quaoar's 3:1 SOR is shown with green lines. Ring detections of Q1R (B. Morgado et al. 2023; C. Pereira et al. 2023; B. Proudfoot et al. 2025) are displayed as shaded red regions (with ring radius and ring width), where darker shading is associated with more numerous ring detections. For realistic values of Quaoar's J_2 (i.e., all except the unconstrained model), Weywot's 6:1 is on the inner edge of the ring, possibly providing a confinement mechanism against inward viscous spreading.

COL variations. Unfortunately, Quaoar is currently in a dense star field, which makes photometry challenging.

6.4. Other Observations to Probe COB-COL Offsets

Aside from higher-fidelity modeling, observations may also provide detailed constraints. Although no telescopes are currently capable of mapping Quaoar's surface, near- and medium-term future telescopes like 30 m class telescopes or the Habitable Worlds Observatory may enable the creation of surface maps, which could correct for Quaoar's COB-COL offset. These are the gold standard for fully correcting for these effects but are unfortunately ∼decades away.

In the shorter term, measurements of COB-COL variations can be feasibly accomplished by using Weywot as a reference. Although the absolute position of Weywot is somewhat uncertain at any given time (based on our poor fit quality), its orbital motion over a short time is generally well constrained. This can be seen in our precise measurement of Weywot's orbital period. Repeated observations of Quaoar and Weywot over a single Quaoar rotation period could reveal COB-COL offsets when subtracting out the predictable motion of Weywot. Although requiring ∼18 hr of continuous observing time, this could sensitively detect periodic COB-COL motion. One drawback to this technique is its insensitivity to the average offset.

Another possible route forward is to use the absolute astrometry of Weywot, obviating the need to use Quaoar's COL as an astrometric reference. This technique has been used to study Pluto's small satellites (S. B. Porter & R. M. Canup 2023). The HST images we use for relative astrometry typically have at least a few Gaia reference stars in each image that could be used for absolute astrometry. Precise absolute astrometry can also be derived from occultations, which are insensitive to Quaoar's COL. We note that our dataset does include occultation-derived relative astrometry, but these are referenced to the ephemeris of Quaoar, which is conditioned upon telescopic observations vulnerable to COB-COL offsets (J. Desmars et al. 2015). Only double

occultations—where both Quaoar and Weywot are detected—completely eliminate COB-COL offsets in relative astrometry. Currently, only one double event has been recorded/published (M. Kretlow 2019; E. Fernandez-Valenzuela et al. 2023), but occultations of Quaoar and Weywot are relatively common. We defer these tasks to future work and encourage ongoing occultation observations of Quaoar and Weywot.

7. Ring Dynamics

With a better understanding of Weywot's orbit, we are able to better characterize Quaoar's rings. Quaoar's outer ring, Q1R, is near both Weywot's 6:1 MMR and Quaoar's 3:1 SOR. Given Quaoar's J_2, Weywot's 6:1 MMR splits into 28 different fifth-order subresonances (C. D. Murray & S. F. Dermott 1999). These are made up of the six eccentricity-only subresonances explored in past works (e.g., B. Morgado et al. 2023; A. Rodríguez et al. 2023), along with 22 mixed eccentricity and inclination subresonances. In an odd-order resonance, there are no inclination-only subresonances at fifth order—although the tenth-order 12:2 resonance does contain inclination-only subresonances.

Typically, inclination/mixed resonances have been ignored for simplicity, but the substantial inclination of Weywot with respect to the ring system suggests their potential importance. The strength of a kth-order inclination subresonance scales with $\sin(i/2)^k$, while eccentricity subresonances scale with e^k. As such, Weywot's inclination of ∼5° is roughly comparable (in terms of resonance strength) with an eccentricity of ∼0.04. This implies that inclination-dominated subresonances may be stronger than eccentricity-dominated/-only subresonances. Inclination resonances are able to excite a variety of interesting phenomena in ring systems. A non-coplanar satellite can induce bending waves and other vertical structure into the rings. Such vertical structure will act to increase the velocity dispersion of the ring particles, potentially helping to suppress accretion.

In Figure 7, we plot the locations of the 28 subresonances based on our two orbits fits—as well as our two comparison

shape models—compared to the ring detections in the literature. Not all of these subresonances will be active, but their radial extent can help better understand the rings. We note that since J_2 is relatively poorly measured, the subresonance locations will not be precisely measured. Based on the radial locations of subresonances from realistic models (top three rows of Figure 7), it is clear that the bulk of Q1R is external to Weywot's 6:1 MMR. Based on our constrained fit, the nominal location of the 6:1 is at 4035 km, with subresonances extending ∼5–10 km on either size. Given Weywot's low eccentricity, the widths of these resonances are extremely small (A. Rodríguez et al. 2023). As such, it is unlikely that Q1R is confined within Weywot's 6:1 MMR. Instead, we suggest that the 6:1 plays a role in confining the inner edge of the ring. As the narrow ring spreads radially due to viscous forces (stemming from particle collisions), the 6:1 may act as a barrier to inward spreading. In contrast, the outer edge of Q1R appears to be bounded by Quaoar's 3:1 SOR. Based on our measurement of Quaoar's mass and a rotation period of 17.752 hr (C. Kiss et al. 2024), Quaoar's 3:1 SOR lies at 4225 km.

In this paradigm, Q1R's arcs remain a mystery. A. Rodríguez et al. (2023) explored whether Weywot could create arcs within Q1R, finding that particles residing in various subresonances can clump together. The subresonances, however, are extremely narrow at Weywot's $e \sim 0.01$, with resonance widths expected to be $\lesssim 1$ km wide (B. Morgado et al. 2023)—much larger than the ∼5 km wide arcs. Likewise, the arcs appear to be further out from the 6:1 subresonances, limiting their use for explaining Q1R's arcs. One possible alternative is the presence of shepherd moons in/near the ring system that maintain the ring's eccentricity and create arcs, much like Galatea's influence on Neptune's Adams ring (F. Namouni & C. Porco 2002; I. De Pater et al. 2018).

At ∼2530 km, Q2R is located near Weywot's 12:1 resonance and Quaoar's 7:5 resonance, at 2543 and 2541 km, respectively. Both of these resonances are high-order, which significantly limits their strength. Detailed simulations should be able to determine at what level these resonances contribute to Q2R's stability/confinement.

With our updated orbit model for Weywot, high-fidelity simulations of Quaoar's rings are now possible. Future work should focus on understanding the confinement of the rings, modeling both MMRs and SORs simultaneously. Simulations should also reflect the non-coplanarity of the system, which could introduce an interesting variety of phenomena like bending waves and/or warping. Outside of understanding the rings' confinement and location, understanding the origin of Q1R's arcs is particularly important. Tracking of the arc's location could reveal the dynamical source of its confinement, even without detecting individual shepherd moons.

8. Conclusions

In this work, we have presented the most comprehensive orbital analysis of the Quaoar–Weywot system to date, leveraging nearly two decades of astrometric data, including new and reanalyzed HST imaging as well as recent stellar occultations. We find the following conclusions.

1. In contrast to past analyses, we find that Weywot's orbit is nearly circular with a robust upper limit of $e < 0.02$.

Weywot is also inclined relative to Quaoar's ring plane, with an inclination of ∼5°.

2. Our modeling incorporates Quaoar's nonspherical gravity field through its J_2 harmonic. We find relatively small values compared to current shape models of Quaoar when assuming that Quaoar's rings lie in its equatorial plane. We interpret this as confirmation that Quaoar is differentiated and calculate a bulk density of 1751 ± 13 (stat.) kg m^{-3} for Quaoar. When relaxing assumptions about Quaoar and the ring's pole alignment, our model appears to overfit the data, providing unphysically large values of J_2.

3. Our orbit models strongly detect COB-COL offsets on Quaoar. These offsets are consistent with latitudinal albedo variations on Quaoar's surface and are necessary to reconcile orbit fits with our dataset of ∼milliarcsecond astrometry. Although modeled here as constant offsets, future work should incorporate physically motivated, time-variable models to better capture the effects of surface heterogeneity.

4. Our measurements of Quaoar's J_2, alongside measurements of Weywot's mean motion and precession rates, allows for detailed determinations of Quaoar's and Weywot's various resonances. We find that Weywot's 6:1 lies just interior to Quaoar's outer ring, while Quaoar's 3:1 SOR lies just exterior to the ring. We propose that these two resonances provide confinement for the ring but are unable to explain the dense arcs of material within the ring. Instead, these arcs may be formed by interactions with shepherd satellites in/near the rings.

5. To facilitate future scientific investigation, we provide an ephemeris of Weywot's position from 2005 to 2035, which can be used to predict Weywot's position to $\lesssim 10$ mas accuracy.

Our findings show that Weywot serves as a sensitive dynamical probe of Quaoar's internal structure and shape, enabling constraints on its gravitational field independent of direct shape modeling. These results further inform our understanding of the formation and confinement mechanisms acting on Quaoar's ring system and reemphasize the importance of non-Keplerian dynamics in trans-Neptunian satellite systems. Future work—including expanded occultation campaigns, absolute astrometry of Weywot, high-resolution imaging of Quaoar's surface, and direct simulations of rings—will be crucial for disentangling the remaining degeneracies and refining models of Quaoar's interior, surface, and ring system.

Author Contribution

B.P. led the overall analysis, writing of the paper, and designing/scheduling of observations and was the principal investigator of the HST program. W.G. analyzed all observations (both new and archival), contributed to interpretation, and provided editing support. D.R. provided access to computing resources, contributed to interpretation, and provided editing support. E.F.V. contributed to occultation interpretation, as well as providing editing support.

ORCID iDs

Benjamin Proudfoot ● https://orcid.org/0000-0002-1788-870X
Will Grundy ● https://orcid.org/0000-0002-8296-6540
Darin Ragozzine ● https://orcid.org/0000-0003-1080-9770
Estela Fernández-Valenzuela ● https://orcid.org/0000-0003-2132-7769

References

Armand, G. 1977, Classical Theory of Desorption Rate Velocity Distribution of Desorbed Atoms; Possibility of a Compensation Effect, SurSc, 66, 321

Bierson, C., & Nimmo, F. 2019, Classical Theory of Desorption Rate Velocity Distribution of Desorbed Atoms; Possibility of a Compensation Effect, Icar, 326, 10

Braga-Ribas, F., Vachier, F., Desmars, J., Margoti, G., & Sicardy, B. 2025, Investigating the Formation of Small Solar System Objects Using Stellar Occultations by Satellites: Present, Future and its Use to Update Satellite Orbits, RSPTA, 383, 20240200

Brown, M. E., & Suer, T. A. 2007, Satellites of 2003 AZ84, (50000), (55637), and (90482), IAUC, 8812, 1

Buie, M. W., Grundy, W. M., Young, E. F., Young, L. A., & Stern, S. A. 2010, Pluto and Charon with the Hubble Space Telescope. II. Resolving Changes on Pluto's Surface and a Map for Charon, AJ, 139, 1128

Buie, M. W., Tholen, D. J., & Grundy, W. M. 2012, The Orbit of Charon is Circular, AJ, 144, 15

Buie, M. W., Tholen, D. J., & Horne, K. 1992, Albedo Maps of Pluto and Charon: Initial Mutual Event Results, Icar, 97, 211

De Pater, I., Renner, S., Showalter, M., & Sicardy, B. 2018, The Rings of Neptune, in Planetary Ring Systems. Properties, Structure, and Evolution, ed. M. S. Tiscareno & C. D. Murray (Cambridge Univ. Press), 112

Desmars, J., Camargo, J., Braga-Ribas, F., et al. 2015, Orbit Determination of Trans-Neptunian Objects and Centaurs for the Prediction of Stellar Occultations, A&A, 584, A96

Dunham, E., Desch, S., & Probst, L. 2019, Haumea's Shape, Composition, and Internal Structure, ApJ, 877, 41

Emery, J., Wong, I., Brunetto, R., et al. 2024, A Tale of 3 Dwarf Planets: Ices and Organics on Sedna, Gonggong, and Quaoar from JWST Spectroscopy, Icar, 414, 116017

Fernandez-Valenzuela, E., Holler, B., Ortiz, J. L., et al. 2023, Weywot: the Darkest known Satellite in the Trans-Neptunian Region, DPS Meeting, 55, 202.04

Foreman-Mackey, D., Farr, W. M., Sinha, M., et al. 2019, Emcee v3: A Python Ensemble Sampling Toolkit for Affine-Invariant MCMC, JOSS, 4, 1864

Fraser, W. C., Batygin, K., Brown, M. E., & Bouchez, A. 2013, The Mass, Orbit, and Tidal Evolution of the Quaoar-Weywot System, Icar, 222, 357

Fraser, W. C., & Brown, M. E. 2010, Quaoar: A Rock in the Kuiper Belt, ApJ, 714, 1547

Fray, N., & Schmitt, B. 2009, Sublimation of Ices of Astrophysical Interest: A Bibliographic Review, P&SS, 57, 2053

Goldreich, P., & Soter, S. 1966, Q in the Solar System, Icar, 5, 375

Grundy, W., Noll, K., Buie, M., et al. 2009, Mutual Orbits and Masses of Six Transneptunian Binaries, Icar, 200, 627

Grundy, W., Noll, K., Buie, M., et al. 2019a, The Mutual Orbit, Mass, and Density of Transneptunian Binary G!kún‖'hòmdímà (229762 2007 UK126), Icar, 334, 30

Grundy, W., Noll, K., Roe, H., et al. 2019b, Mutual Orbit Orientations of Transneptunian Binaries, Icar, 334, 62

Grundy, W., Noll, K., Virtanen, J., et al. 2008, (42355) Typhon Echidna: Scheduling Observations for Binary Orbit Determination, Icar, 197, 260

Grundy, W., Porter, S., Benecchi, S., et al. 2015, The Mutual Orbit, Mass, and Density of the Large Transneptunian Binary System Varda and Ilmarë, Icar, 257, 130

Ikeya, R., & Hirata, N. 2024, Gravitational Disturbance on Asteroidal Ring Systems by Close Encounter with a Small Object, Icar, 418, 116153

Kiss, C., Müller, T., Marton, G., et al. 2024, The Visible and Thermal Light Curve of the Large Kuiper Belt Object (50000) Quaoar★, A&A, 684, A50

Kretlow, M. 2020, Beyond Jupiter - (50000) Quaoar, JOA, 10, 24

Krist, J. E., Hook, R. N., & Stoehr, F. 2011, 20 Years of Hubble Space Telescope Optical Modeling using Tiny Tim, SPIE, 8127, 166

Langmuir, I. 1913, The Vapor Pressure of Metallic Tungsten, PhRv, 2, 329

Luger, R., Agol, E., Foreman-Mackey, D., et al. 2019, Starry: Analytic Occultation Light Curves, AJ, 157, 64

Margoti, G. 2024, Determinação da Forma Tridimensional de (50000) Quaoar Por Ocultações Estelares Utilizando Algoritmo Genético Para Minimização, MA thesis, Univ. Tecnológica Federal do Paraná

Morgado, B., Sicardy, B., Braga-Ribas, F., et al. 2023, A Dense Ring of the Trans-Neptunian Object Quaoar Outside its Roche Limit, Natur, 614, 239

Murray, C. D., & Dermott, S. F. 1999, Solar System Dynamics (Cambridge Univ. Press)

Namouni, F., & Porco, C. 2002, The Confinement of Neptune's Ring Arcs by the Moon Galatea, Natur, 417, 45

Noviello, J. L., Desch, S. J., Neveu, M., Proudfoot, B. C., & Sonnett, S. 2022, Let It Go: Geophysically Driven Ejection of the Haumea Family Members, PSJ, 3, 225

Ortiz, J., Gutiérrez, P., Sota, A., Casanova, V., & Teixeira, V. 2003, Rotational Brightness Variations in Trans-Neptunian Object 50000 Quaoar, A&A, 409, L13

Pereira, C., Sicardy, B., Morgado, B., et al. 2023, The two Rings of (50000) Quaoar, A&A, 673, L4

Porter, S. B., & Canup, R. M. 2023, Orbits and Masses of the Small Satellites of Pluto, PSJ, 4, 120

Proudfoot, B., Holler, B., Arimatsu, K., et al. 2025, Constraints on Quaoar's Rings and Atmosphere from JWST/NIRCam Observations of a Stellar Occultation, PSJ, 6, 146

Proudfoot, B., & Ragozzine, D. 2021, Prolate vs Oblate: When Do Sectoral Gravitational Harmonics Matter, AAS/DDA Meeting, 53, 107

Proudfoot, B. C. N., Ragozzine, D. A., Giforos, W., et al. 2024a, Beyond Point Masses. III. Detecting Haumea's Nonspherical Gravitational Field, PSJ, 5, 69

Proudfoot, B. C. N., Ragozzine, D. A., Thatcher, M. L., et al. 2024b, Beyond Point Masses. II. Non-Keplerian Shape Effects are Detectable in Several TNO Binaries, AJ, 167, 144

Ragozzine, D., & Brown, M. E. 2009, Orbits and Masses of the Satellites of the Dwarf Planet Haumea (2003 EL61), AJ, 137, 4766

Ragozzine, D., Pincock, S., Proudfoot, B. C., et al. 2024, Beyond Point Masses. I. New Non-Keplerian Modeling Tools Applied to Trans-Neptunian Triple (47171) Lempo arXiv:2403.12785

Rodríguez, A., Morgado, B., & Callegari, N. 2023, Dynamical Characterization of the 6/1 Mean Motion Resonance between Quaoar's Ring and Weywot, MNRAS, 525, 3376

Scheeres, D., Williams, B. G., & Miller, J. K. 2000, Evaluation of the Dynamic Environment of an Asteroid: Applications to 433 Eros, JGCD, 23, 466

Schörghofer, N. 2022, Statistical Thermodynamics of Surface-Bounded Exospheres, EM&P, 126, 5

Sicardy, B., Renner, S., Leiva, R., et al. 2020, The Dynamics of Rings Around Centaurs and Trans-Neptunian Objects, in The Trans-Neptunian Solar System, ed. D. Prialnik, M. Barucci, & L. Young (Elsevier), 249

Tholen, D. J., & Buie, M. W. 1997, The Orbit of Charon, Icar, 125, 245

Vachier, F., Berthier, J., & Marchis, F. 2012, Determination of Binary Asteroid Orbits with a Genetic-based Algorithm, A&A, 543, A68

Yoder, C. F. 1995, Astrometric and Geodetic Properties of Earth and the Solar System, in Global Earth Physics A Handbook of Physical Constants, ed. Thomas Ahrens (American Geophysical Union), 1

Young, E. F., Galdamez, K., Buie, M. W., Binzel, R. P., & Tholen, D. J. 1999, Mapping the Variegated Surface of Pluto, AJ, 117, 1063